ELSEVIER

Contents lists available at ScienceDirect

### **Chemical Engineering Science**

journal homepage: www.elsevier.com/locate/ces



# Experimental investigation of fluid flow around a porous cube for Reynolds numbers of 400–1400



Likun Ma<sup>a,b</sup>, Sina Kashani<sup>c</sup>, Xue Li<sup>a</sup>, Shuliang Xu<sup>a</sup>, David S. Nobes<sup>c,\*</sup>, Mao Ye<sup>a,\*</sup>

- a National Engineering Research Center of Lower-Carbon Catalysis Technology, Dalian Institute of Chemical Physics, Chinese Academy of Sciences, Dalian 116023, China
- <sup>b</sup> University of Chinese Academy of Sciences, Beijing 100049, China
- <sup>c</sup> Department of Mechanical Engineering, University of Alberta, Edmonton T6G 1H9, Canada

#### HIGHLIGHTS

- PIV experiments of the fluid flow around a porous cube for Re = 400 1400 were conducted.
- Wake recirculation for porous cube enlarged due to push effect of penetration flow.
- Drag coefficients of porous cube higher than that of its solid counterpart at larger Re.
- Porous structure and shape of catalyst alter the hydrodynamics in industrial reactors.

#### ARTICLE INFO

#### Article history: Received 10 September 2022 Received in revised form 6 November 2022 Accepted 30 December 2022 Available online 2 January 2023

Keywords:
Porous cube
Particle Image Velocimetry
Wake characteristics
Drag coefficients

#### ABSTRACT

Porous particles with different shapes are commonly used in chemical reactors. Flow characteristics and drag coefficients of these porous particles, affecting heat and mass transfers essentially, have received less attention at the single particle level. This work provides the particle image velocimetry investigation of flow around a porous cube with Darcy number  $Da = 1.52 \times 10^{-3}$  and Reynolds numbers Re = 400 - 1400. It is found that the recirculation region behind the porous cube is significantly enlarged compared with that behind its solid counterpart owing to the strong push effect of penetration flow. Meantime, drag coefficients of the porous cube appear to be much higher than that of the solid cube at larger Re. This might be due to the transition of external flow to internal flow through the porous cube in the presence of permeability on the one hand, and the existence of rough surface of porous cube on the other hand.

© 2022 Elsevier Ltd. All rights reserved.

#### 1. Introduction

Porous particles with different shapes are commonly used in industrial chemical processes (Wang, 2020; Zhu et al., 2021). One of the typical examples is fixed-bed reactors (Jurtz et al., 2019), which are widely utilized in methane steam reforming, ethylene epoxidation, maleic anhydride production, and among many others (Dixon et al., 2012). Fluid flows around porous catalyst particles can significantly affect the mass transfer, heat transfer and reaction in fixed bed reactors (Augier et al., 2010). Thus, the hydrodynamics in fixed bed reactors with porous catalyst particles plays an important role in improving and optimizing reactor design (Bai et al., 2009).

In the past, a vast amount of experimental and simulation research has been conducted to study the pressure drop

E-mail addresses: dnobes@ualberta.ca (D.S. Nobes), maoye@dicp.ac.cn (M. Ye).

(Atmakidis and Kenig, 2009), flow field (Bai et al., 2009) and mean drag coefficient  $C_D$  (Reddy and Joshi, 2008) in fixed beds. It should be noted that  $C_D$  is the dimensionless drag force defined as  $C_D = F/(0.5\rho u^2 A)$ , in which F is the drag force,  $\rho$  is the density of fluid, u is the flow velocity of bluff body relative to the fluid, and A is the reference area. It was also observed that the hydrodynamics of fluid flow, which is closely associated with drag force (Mazaheri et al., 2012), can be affected by the permeability of porous structures (Guo et al., 2021) and topology of fixed spherical particles arrangements (Topic et al., 2022). However, most of these studies were carried out at reactor-level and focused on the macroscopic fluid flows in the beds. Fundamentally, it is highly desired to understand how the porous nature of catalyst particles affects the interaction between the fluid flow and particle at single particle-level.

Fluid flow around a single porous particle has been either theoretically or numerically studied by many researchers. Neale et al. (1973) theoretically studied creeping flow past an isolated porous

<sup>\*</sup> Corresponding authors.

sphere and found the drag on a porous sphere is less than that of a solid sphere at a low Reynolds number ( $Re = du\rho/\mu$ , where d is the characteristic length of the sphere and  $\mu$  is the dynamic viscosity of the fluid). Joseph and Tao (1964) analyzed the low Re viscous liquid flow past a porous sphere and showed that the permeability effect on the drag is equivalent to the reduction of the sphere radius. Shahsavari et al. (2014) numerically simulated flow through a porous circular cylinder symmetrically located between two solid parallel plates and discovered that the flow interception efficiency and streamlines varied with the Darcy numbers ( $Da = k/D^2$ , where k is permeability and D is the characteristic length of the porous body). Novmer et al. (1998) investigated the fluid flow past permeable cylinders for Re of 10, 100 and 1000 with numerical simulations. They found that the drag approaches zero at the upper limit of permeability because the fluid can pass through with the least resistance, while at low permeability (i.e.  $Da = 10^{-6}$ ) the drag approximates that of a solid cylinder since little fluid can flow through (Bhattacharyya et al., 2006). In between these two extremes of the permeability, drag coefficients manifest complex behaviors dependent on Re. Bhattacharyya et al. (2006) conducted a numerical simulation for flow around a porous circular cylinder with  $Re = 1 \sim 40$  and  $Da = 10^{-6} \sim 1.5$ . It was shown that wake length decreased with an increasing Da for the porous cylinder owing to the shift of separation point downstream, in which the streamlines and vorticity patterns are different from those of solid cylinders. They observed that the drag coefficient at  $Da = 10^{-3}$  and  $10^{-2}$  are less than that at  $Da = 10^{-6}$  (Bhattacharyya et al., 2006). Wu and Lee (1999) numerically studied the flow field around a highly porous sphere moving through a circular tube for  $0.1 \le Re \le 40$ . It was found  $\beta$  ( $\beta = 0.5D/\sqrt{k}$ ) of the porous sphere could markedly affect the hydrodynamic drag, and no boundary layer separation occurred at the rear of the porous sphere at a large Re when the permeability of the sphere becomes high. Yu et al. (2011) numerically investigated flow around a porous circular cylinder with the Reynolds number  $Re = 10 \sim 40$  and found that the critical Re for the onset of recirculating wake is lower than that of its solid counterpart. Jain and Basu (2012) simulated the fluid flow past a porous sphere for  $Re = 0.1 \sim 1000$  and observed the presence of recirculation flows and back flows inside the porous sphere at Re = 1000 and  $Da = 3 \times 10^{-4}$ , which could also impact the external flow fields. Meanwhile, drag coefficients of porous spheres are found to be greater than those of impermeable spheres for the intermediate ranges of permeability at a specific Re value due to the formation of circulating cells and back flows within porous spheres. Wittig et al. (2017) simulated flows past a porous sphere over  $Re = 10 \sim 450$  and showed that the drag coefficients of porous spheres were significantly influenced by different porosities.

Despite the aforementioned theoretical and numerical investigations, only a few experimental works have been carried out to study the fluid flow around a single porous particle. One of the earliest experimental studies on porous spheres was conducted by Matsumoto and Suganuma (1977), in which they first showed that the effect of permeability on drag coefficients cannot be neglected at higher permeability in the low Re regime. Later on, Masliyah and Polikar (1980) experimentally measured drag coefficients of a porous sphere for  $Re = 0.2 \sim 120$ . They found that the theoretical results of Neale et al. (1973) hold for low Re, but a larger drag was achieved at higher Re compared with the results of a solid sphere. Emadzadeh and Chiew (2016) used particle image velocimetry (PIV) to measure the settling of porous spheres at  $Re = 1 \sim 10000$ , suggesting a significantly higher  $C_D$  is achieved for  $\textit{Re} = 1000 \sim 10000$  compared with solid spheres. They also found the evolution of wake as well as the flow field is clearly different. Later, based on particle tracking velocimetry (PTV) and PIV experiments, they further found that, for  $Re \geq 100$ ,  $C_D$  of a porous sphere is significantly higher than that of its nonporous counterpart at a same Re, which may be due to the complicated interplay between the surface roughness effects, permeability effects, alterations of wake regions, and boundary layer separation (Emadzadeh and Chiew, 2020). In a PIV study by Takeuchi et al. (2007), they observed the reattachment point of the porous cylinder displaces several times as that of the solid cylinder in presence of the permeability, affecting the vortex shedding in the near field. Recently, we used Support Vector Machine to find the most important features affecting drag force of porous spheres based on the data of sedimentation experiments, in which the permeability was identified in addition to the solid fraction  $\phi$  and Re (Ma et al., 2022a).

It can be found that most of the studies discussed above concentrate on the porous circular cylinder/sphere. The circle/sphere has omnidirectional symmetry and can be regarded as the simplified ideal geometric shape. However, in practice, most of catalyst particles have non-ideal shapes (Martin, 1981; Wei and Zhu, 2019; Zhong et al., 2016). In this work, we will therefore carry out a PIV study to understand the effects of permeability on flow characteristics and drag coefficients of a porous cube. The model cubic particle is motivated by a newly developed fixed bed catalyst that is of cubic and porous nature. The study of flow around solid cuboids already showed that the sharp edges and discontinuous symmetry of cuboids can lead to different wake characteristics uncommon for smooth surface bluff bodies (e.g. the circle/sphere) (Khan et al., 2018). Despite the model particle, Re considered in this work also follows the fixed bed reactor operation. For comparison, parallel experiments with a solid cube of similar size were also carried out. We expect the experimental results can provide some insights into the combined impacts of the permeability and particle shape on fluid flow around a single porous particle of industrial interest.

#### 2. Experimental setup

In the present study, PIV was used to measure flow fields around the solid and porous cube for different Re. PIV measurements were conducted in a water tank with a testing section of  $400 \times 500 \text{ mm}^2$  cross-section and a length of 1200 mm. The measurement system employed in this work is schematically shown in Fig. 1a, and a detailed description can be found in Ma et al. (2022b). A double-pulse Nd:YAG laser (Model Solo III-15z, New Wave; energy: 50 mJ/pulse, wavelength 532 nm) was used to illuminate seeding particles (Hollow glass spheres of size 18 µm). A 14-bit double-frame CCD camera (Model Imager Pro X 4 M, LaVision; image size:  $2112 \times 2072$  pixels) was used to capture images of the fluid flow. The acquisition frequency of the camera was double-frame rate of 5.05 Hz. A solid or porous cube were fixed to a traverse (VELMEX. Inc.) along with the camera which could move with a constant velocity to provide a certain Reynold number in the horizontal direction. The data images are collected in a Eulerian reference frame moving with the cube. The laser sheet passed through the central plane of the cube. The camera's fields of views were about 5 times the cube's characteristic length to ensure the capture of wake characteristics in freestream directions. A crosscorrelation algorithm was used to calculate vector fields based on raw PIV fluid images after sliding minimum subtraction and min-max filter for intensity normalization. The cross-correlation algorithm were carried out by using interrogation window sizes of  $64 \times 64$  pixels with 50% overlap for the first pass and  $32 \times 32$ pixels with 50% overlap for the second pass.

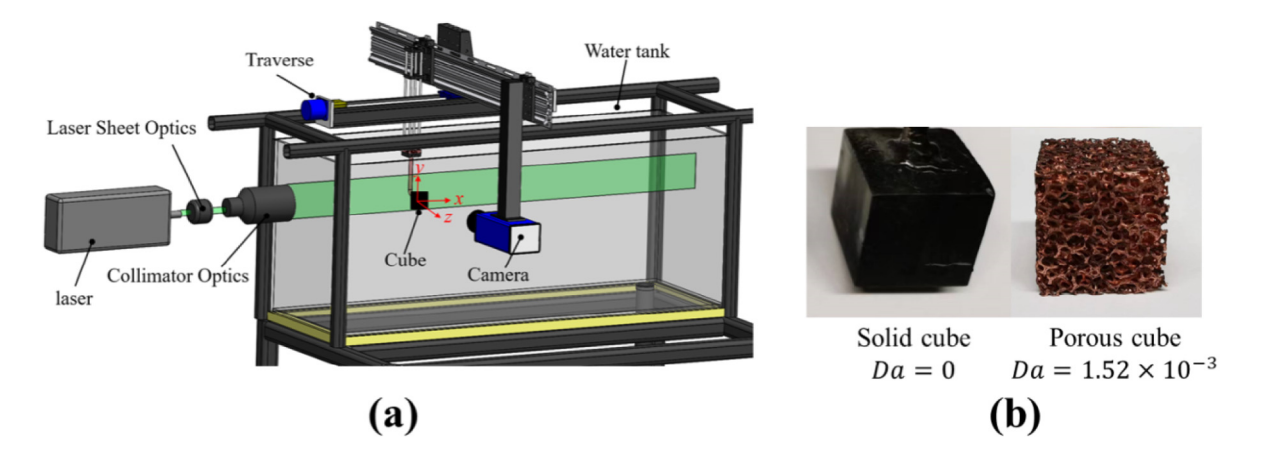


Fig. 1. (a) Schematic of the PIV setup. (b) Snapshot of the solid and porous cube.

A solid and porous cube with an edge length of 30 mm were employed in the measurements, as shown in Fig. 1b. The choice of the parameters of these two model cubes follows the catalyst used in the fixed bed reactor. For a single practical catalyst cube, it has an equivalent diameter D of  $\sim 5$  mm and is formed with many monomer grains of  $d = 300 \,\mu\text{m}$ . The porosity  $\varepsilon$  of the catalyst is  $\sim 90$  %. According to the expression for permeability  $k = (\varepsilon^3 \times d^2)/(180 \times (1 - \varepsilon)^2)$  and  $Da = k/D^2$ , the Da $1.46 \times 10^{-3}$  is calculated. Also, based on the typical operation conditions of the fixed reactor, we estimate that Re for the catalyst cube is  $\sim$  507. Because porous cubes made of foam metals can provide suitable permeability and porosity for this specified work (Noymer et al., 1998), the porous cube in the experiments was made of foam metal, with  $Da = 1.52 \times 10^{-3}$ , close to the practical catalyst cube. The range of Re for fluid flow around the cube is of  $400 \sim 1400$ . Note that here, all Re were defined based on the edge length of the cube. Also, the solid cube in the experiments was made by 3D printing with a Darcy number of 0.

Sample flow fields for solid and porous cube are shown in Fig. 2 to illuminate some definitions used in this work. As can be seen from Fig. 2,  $u_{\infty}$  is the freestream velocity at the upstream of the bluff body. The coordinate system was chosen such that the origin (0,0) is at the center of the solid and porous cube. Field of view (FOV) for the wake is marked by a red dashed box. The wake region is the recirculation zone and wake length is defined as the distance between the stagnation point position to the cube center. The positions of the stagnation points were identified by searching for the local minimum velocity position in the flow field near the rear of the recirculation zone. For the experiments with Reynolds number of Re = 400 - 1400, the instantaneous flow fields for flow around the cube are essentially unsteady flow (Saha, 2004), and the wakes are unstable with wake shapes changing all the time. According to the experimental results of wake lengths of time-averaged streamlines in the present work, it is shown that the length of five times the cube edge (i.e. x = 5D) is long enough to capture almost all wake characteristics and flow structures in both instantaneous and time-averaged flows under the investigated Re conditions.

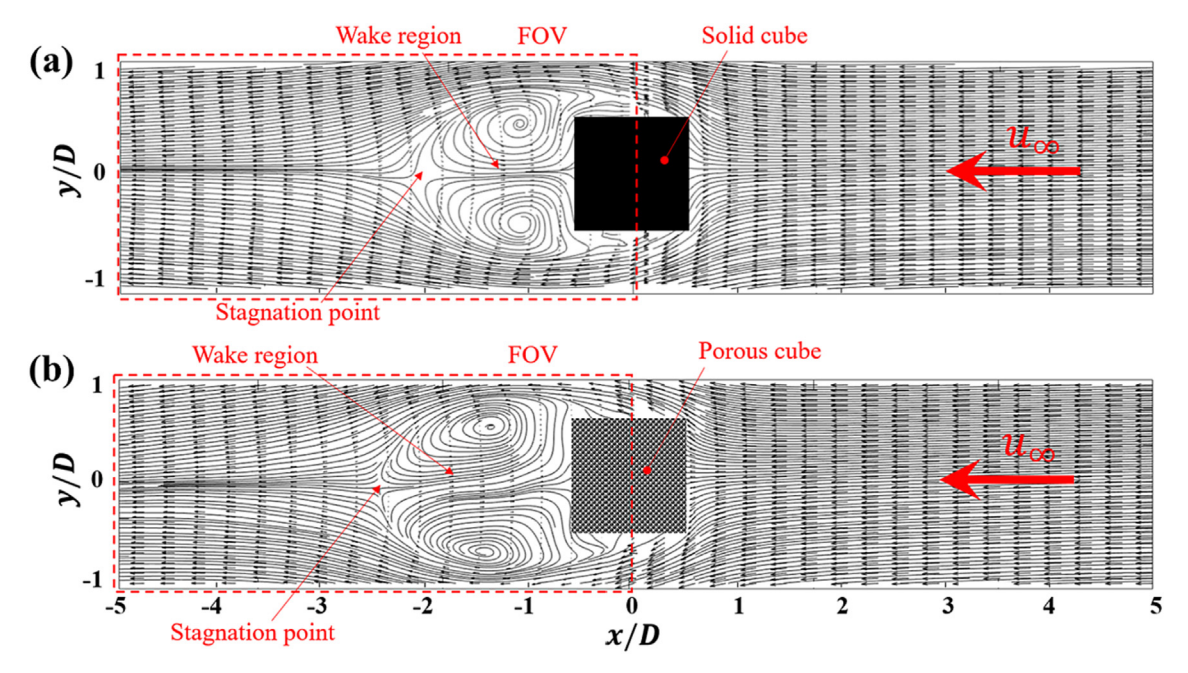


Fig. 2. Samples of flow fields for (a) solid cube and (b) porous cube.

Thus, in this study, the measured area of the wake for the cube is nearly up to 150 mm, which is  $\sim$  5 times the length scale of the cube. In the following sections, x and y have been normalized by the side length of the cube and all positions are normalized positions x/D and y/D with x, y being absolute positions and D being the diameter of cubes. In this work, for each Re, the number of image pairs/instantaneous flow fields used for processing is set to be at least 500. In the experiments, instantaneous flow fields from the initial time of wake formations to the fully developed stages were fully recorded. But only the instantaneous images of the fluid flows at the fully developed stage were used to calculate time-averaged flow fields. Different frame numbers of images to derive the time-averaged flow properties and vorticity were tested and it was found that 200 frames are enough to ensure a reliable time-averaged flow field. Therefore, for all Re, at least 200 frames of instantaneous images of flow fields at the fully developed stages were used to calculate the mean flow properties and vorticity in the present work. As illumination of the field of view was only from one side, the full average velocity flow field around the cube as shown in Fig. 2 was generate by first capturing the wake flow of the cube followed by the leading flow as the cube traveled in the opposite direction. These two average flow fields were then mapped onto a single Eulerian average of the entire flow around the cube.

#### 3. Results and discussions

Flows past a porous cube with  $Da=1.52\times 10^{-3}$  measured by PIV were conducted for Re=400,600,800,1000,1200,1400 to investigate the flow characteristics and drag coefficients in the wake. For comparisons, flows past a solid cube with Da=0 were also carried out for the same Reynolds numbers, allowing the experimental method to be validated. Then, the instantaneous wake velocity behaviors, time-averaged wake velocity behaviors including whole-field streamlines and velocity profiles along streamwise locations for different Re, vorticity field distributions and drag coefficients are respectively presented in following sections.

#### 3.1. Validation of experiment method

The experimental setup of PIV and the data processing method in the present work were validated by comparing experimental

results for the case of the solid cube in the present work with experimental works of wake sizes (Khan et al., 2018) and drag coefficients (Hölzer and Sommerfeld, 2008; Khan et al., 2018) available in the literature. As can be seen from Fig. 3(a), wake lengths for the solid cube in the present work agree well with those in Khan et al. (2018) except for Re = 800. This deviation can be explained by the aberrant phenomena that Khan et al. (2018) found. Khan et al. (2018) found there is an aberration at Re = 785 for the solid cube, and recirculation regions increase till Re = 785 and then decrease at a higher Re, indicating a possible transition at Re = 785. Hence, there is a deviation between the stagnation point position of our work at Re = 800 and that of Khan et al. (2018) at Re = 785. The modified wake survey method (Bohl and Koochesfahani, 2009), the detailed description of which is provided in Section 3.2.3, was used to obtain drag coefficients based on experimental flow fields. In Fig. 3(b), it was shown that drag coefficients calculated by the modified wake survey method (Bohl and Koochesfahani, 2009) based on our experimental flow fields for solid cube are also consistent with those obtained in Khan et al. (2018) as well as Hölzer and Sommerfeld (2008), which further validates the reliability of the experimental setup of PIV and the data processing method in the present work.

#### 3.2. Flow around a porous cube

Typical experimental results with time-dependent instantaneous flow fields with twelve sequential time steps (2.38 s) at Re=1200 for fluid flows around both the solid and porous cube are shown in Fig. 4(a) and (b), respectively. The origin (0,0) is at the center of the cubes, and the direction of the freestream  $u_{\infty}$  is annotated in Fig. 4. As shown in Fig. 4, vortexes can be created behind both the solid and porous cube when the shear layer rolls and separates at the cube edges. Compared with the solid cube, a larger recirculation region behind the porous cube is formed with three, four, five or more smaller vortex centers. As time evolves, small vortices will diffuse in the fluid flows. Khan et al. (2018) showed that the flow with more small pockets of recirculating regions may be due to the high momentum of the flows which can break down the rolling shear layers and carry it into the wake.

Flow separation at the leading edge of the porous cube is different from that of the solid cube due to the porous permeable edge which can cause a reduction of surface curvature/sharpness. Mean-

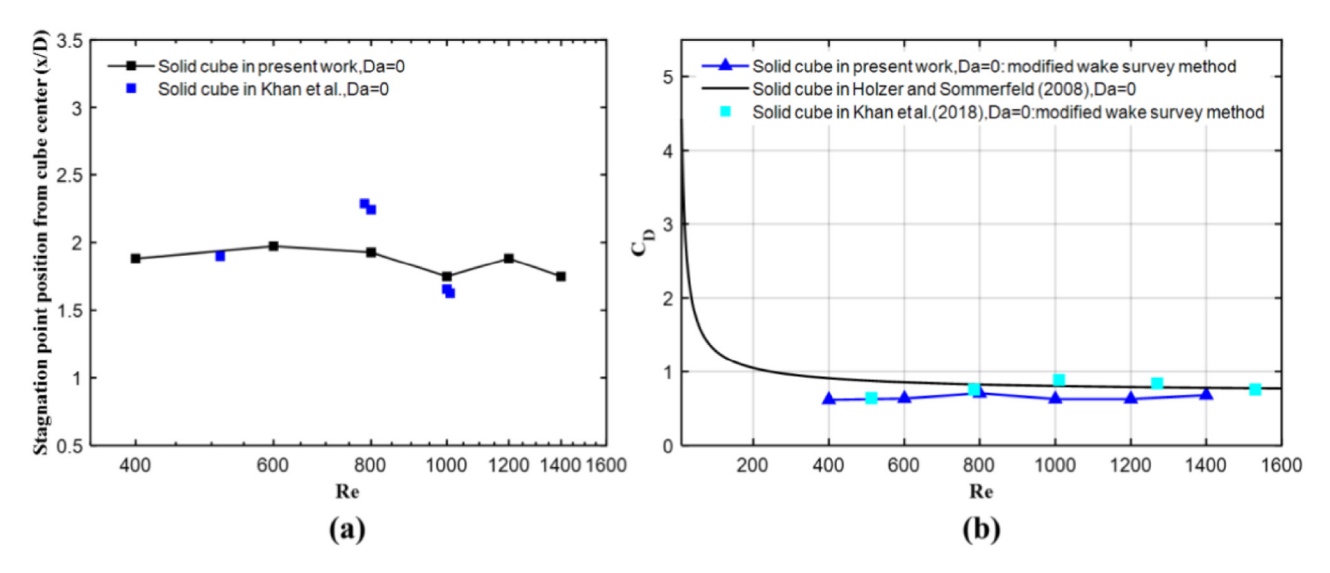


Fig. 3. Comparisons of (a) wake lengths, (b) drag coefficients for the solid cube in the present work and results in the literature.

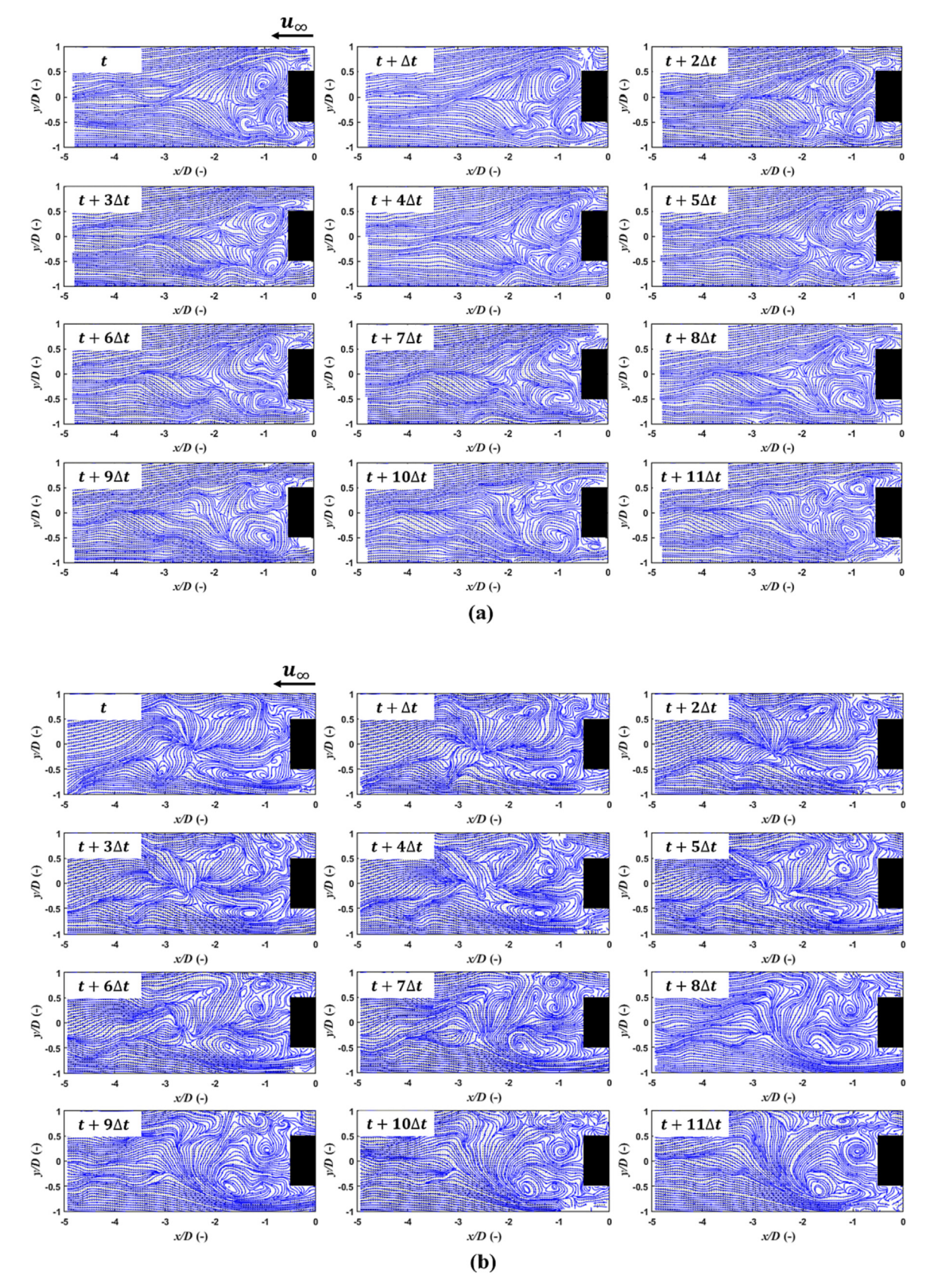


Fig. 4. Temporal variation of instantaneous streamlines in 2.38 s ( $\Delta t = 0.198$  s) behind flow around the (a) solid cube and (b) porous cube at Re = 1200.

while, penetration of the flow passing through the porous cube can also affect the wake regions. As found by Bhattacharyya et al. (2006), in contrast to the solid cylinder, the porous cylinder can

allow a finite amount of fluid to pass through it and velocities of the penetration fluid at the interface increase with the increase of *Da*, which can reduce the relative importance of the inertial forces in the external flow field and lead to a delay in flow separation, corresponding to a reduced *Re*. As streamlines can pass through the bluff body, the normal velocity component is nonzero at the surface, which resembles the flow around a solid bluff body with base bleed (Yu et al., 2010). On the one hand, a decrease of the external fluid flow around the porous cube can cause a reduction of the flow *Re*, which corresponds to a smaller wake region. On the other hand, the penetration flow through the porous cube can push the wake region downstream, which corresponds to a larger wake region. Hence, the present work tries to provide some insights into the competition and/or cooperation of all above-mentioned mechanisms to illuminate the effect of permeability described by *Da* for a porous cube.

## 3.2.1. Effect of Darcy number on time-averaged velocity field distributions

Time-averaged flow fields were calculated based on sufficient instantaneous flow fields. Time-averaged streamlines for flow around the solid cube and porous cube at Re=1200 are shown in Fig. 5. It can be observed that the small and weak vortices in instantaneous streamlines in Fig. 4 are washed away upon time-averaging the flow as shown in Fig. 5(b). It was shown from the streamline patterns for the range of Reynolds number considered in this study that the recirculation regions form at the downstream side of the porous cube, consisting of two vortices in the wake.

A large permeability means more void volume within the bluff body for fluids to past through and streamlines penetrate the porous region more easily when Da is high. As can be seen from Fig. 5, the wake size of the porous cube is significantly larger than that of the solid cube, which can be contributed to the strong penetration flow based on the large permeability  $Da = 1.52 \times 10^{-3}$ . The force of the penetration flow can press the downstream vortex downstream and push the stagnation point downstream with a shift to the left in Fig. 5. It can also be clearly seen from zones A and A' in Fig. 5(a) that side vortexes of the solid cube near the side edge are significant, while side vortexes for the porous cube in zones B and B' in Fig. 5(b) are almost negligible due to the impact of the penetration flow on the porous side edges and the decrease of surface curvature for porous edges.

The visualizations of the recirculation regions in Fig. 5 give a qualitative vision of the flow fields for flow past the solid and porous cube. A quantitative result which is characterized by non-dimensional time-average streamwise velocity profiles is provided in Fig. 6. The streamwise velocity profiles along  $-1 \le y/D \le 1$  at different streamwise locations x/D = 1, 2, 3 for flow around the solid cube and porous cube at all investigated Re are respectively carried out. As can be seen from Fig. 6(a) and (b), the presence of negative velocities at streamwise locations x/D = 1 and x/D = 2 illuminates the presence of the recirculation region, while for x/D = 3, as shown in Fig. 6 (c), there is no negative velocity indicating the end of the recirculation region, and the velocities in the recirculation

wake region are recovered after a few x/D positions. As Fig. 6(b) and (c) show, the porous cube has larger  $u_x$  profiles than those of the solid cube for both x/D = 2 and x/D = 3 at Re = 600, 800, 1000, 1200, 1400 indicating larger recirculation wake sizes, which are due to the presence of the strong penetration flow. For x/D = 1, as can be seen from Fig. 6(a), the magnitude of the velocity profiles for the cases of the porous cube and solid cube are almost same because the locations of x/D = 1 are within the recirculation wake.

The lengths of the recirculation regions vary with Re are summarized in Fig. 7, which shows flow behavior, especially the wake size, is a function of the Reynolds number as well as the Darcy number. As Fig. 7 shown, the size of the recirculation region for the porous cube is almost the same as that of the solid cube at Re = 400, while for 600 < Re < 1400, sizes of the recirculation regions for the porous cube are significantly increased compared with those of the solid cube. It can be concluded that, for a large permeability of  $Da = 1.52 \times 10^{-3}$  as used here, the push effect of the penetration flow through the porous cube which can press the vortex downstream is stronger than the reduction effect of the flow Re due to the decrease of external fluids flow around the porous cube. This corresponds to a larger wake region for a high-permeability porous cube. For the investigated Re range  $400 \le Re \le 1400$ , the size of the recirculation region doesn't increase in size with an increase in Reynolds number as expected. It can be explained that for the intermediate Re studied in the present work, the recirculating zones get a lower amount of time to grow in size for a larger Re due to vortex shedding, and will detach as observed at a lower Re where the recirculating region is larger (Khan et al., 2018).

## 3.2.2. Effect of Darcy number on time-averaged vorticity field distributions

For porous bodies, the penetration flow and the reduction of surface curvature/sharpness can also affect the vorticity field. Additionally, for flow past the porous bodies, researchers have found that the appearance of the recirculating wake at a finite Reynolds number should be viewed as the consequence of vorticity accumulation (Yu et al., 2010; Yu et al., 2011) rather than the result of the separation process described by boundary-layer theory (Leal, 1989). These new findings inspire us to study the vorticity field of the porous cube to assist in shedding light on the wake phenomena.

The vorticity  $\omega$  is calculated based on the curl of the velocity by  $\omega = \nabla \times u = \left(\frac{\partial u_y}{\partial x} - \frac{\partial u_x}{\partial y}\right) \widehat{e}_z$ , where  $u_x$  and  $u_y$  are respectively the velocity components in the streamwise direction and vertical direction. The vorticity contours for the solid and porous cube at Re = 1200 are shown in Fig. 8. As can be seen, the vorticity is accumulated from the leading edges of both the solid cube and porous cube, and the recirculating wakes are induced when the accumulated vorticity is sufficiently strong. Two opposite vortices are

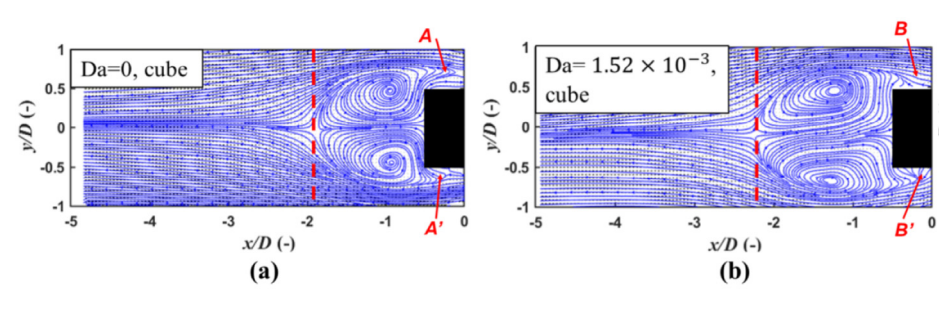


**Fig. 5.** Streamlines for flow around (a) the solid cube and (b) the porous cube at Re = 1200.

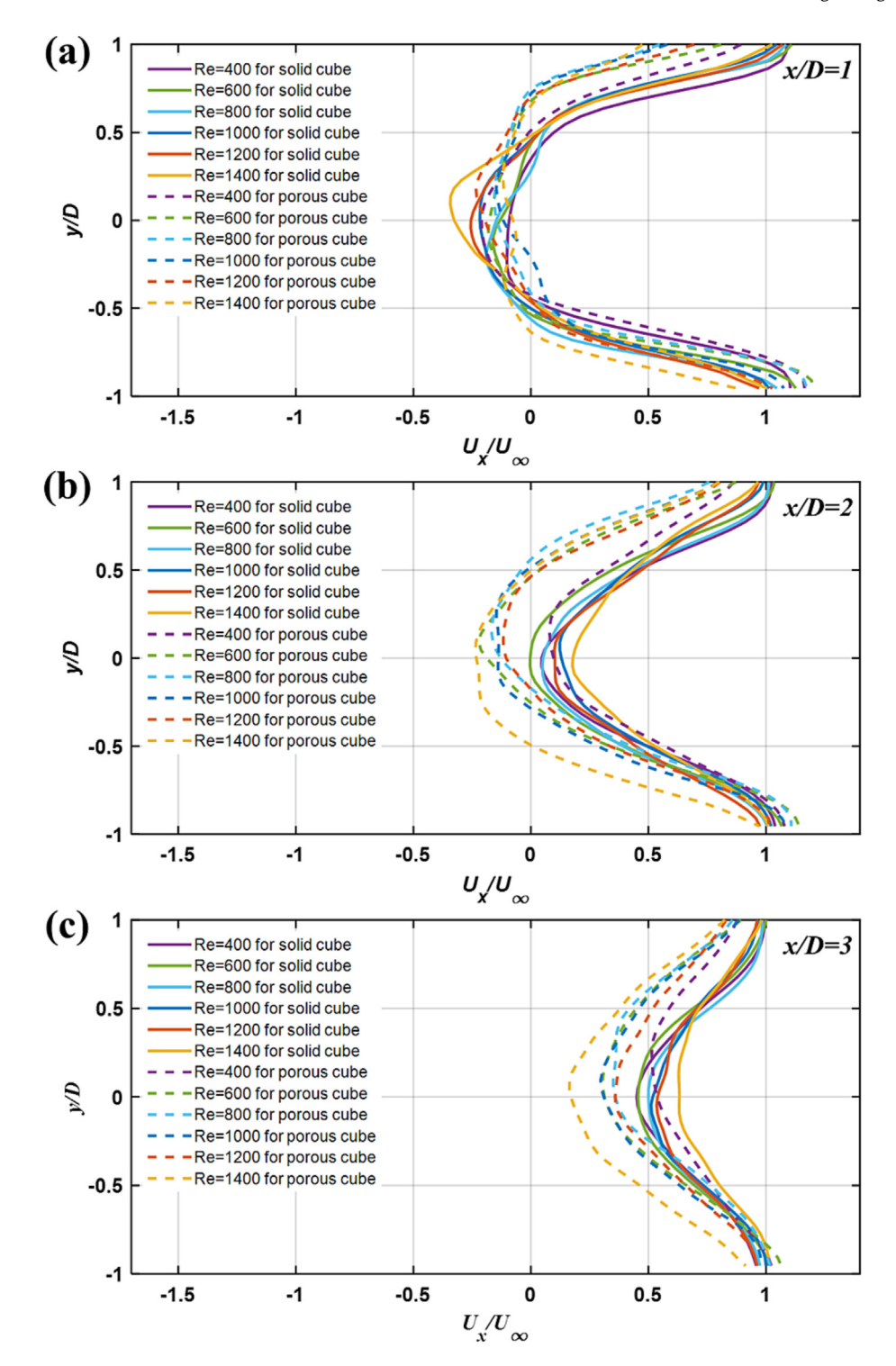


**Fig. 6.** Non-dimensional time-average streamwise velocity profile at different streamwise locations x/D = 1, 2, 3 for flow around the solid cube and porous cube at Re = 400, 600, 800, 1000, 1200, 1400.

formed at the downstream side of both the solid and porous cube. The vorticity diffuses from the external surface into the external flow field for the solid cube, while for the porous cube, the vorticity can diffuse into both the external flow fields and the internal flow fields. The rotational effects slowly die as the flow moves farther downstream due to the diffusion. How the vorticity disperses out along various streamwise locations x/D for all Re is shown in Fig. 9, which provides the maximal and minimal values of vortices at different streamwise locations x/D (Note: maximum vortices is

for positive values of vorticity at each x/D, and minimum vortices is for negative values of vorticity at each x/D) for flow around the porous cube and solid cube. The vorticity near the rear of the cube, which is around  $x/D \sim -0.5$ , shows a maximal vorticity among the whole flow field for both the solid and porous cube at all Re considered, and farther downstream it will converge to zero due to the diffusion. Values of the vorticity at all Re for both solid and porous cube initially increase with Re increasing for the range of  $Re = 400 \sim 800$ . When Reynolds number is more than 800, the

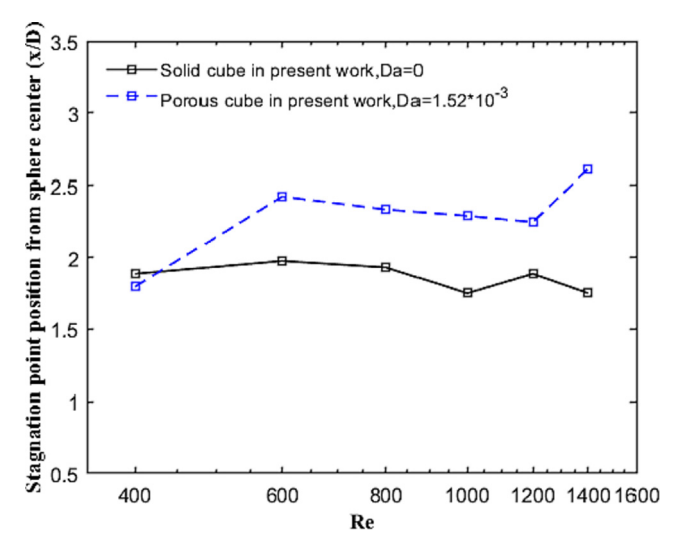


Fig. 7. Comparisons of wake lengths between the porous and solid cube.

vorticity shows a significant decrease and then it gradually increases again with Re increasing, causing the weakest vorticity at Re = 1000 for both the solid and porous cube. The variation of vorticity at Re = 800 may be associated to aberrant phenomena at Re = 785 that Khan et al. (2018) found, in which the recirculation region increases till Re = 785 and then decreases at a higher Re, indicating a possible transition range of flow around  $Re \sim 785$ .

## 3.2.3. Comparisons of drag coefficients between the porous cube and the solid cube

Based on the PIV measurement flow fields, which was obtained by a non-intrusive manner without instrumentation interference, drag coefficients based on PIV experimental measurements can be calculated from the integral momentum theorem.

Drag coefficients can be estimated by the classical wake survey method (Bohl and Koochesfahani, 2009) based on the time-average streamwise velocity profile in the wake, in general described by:

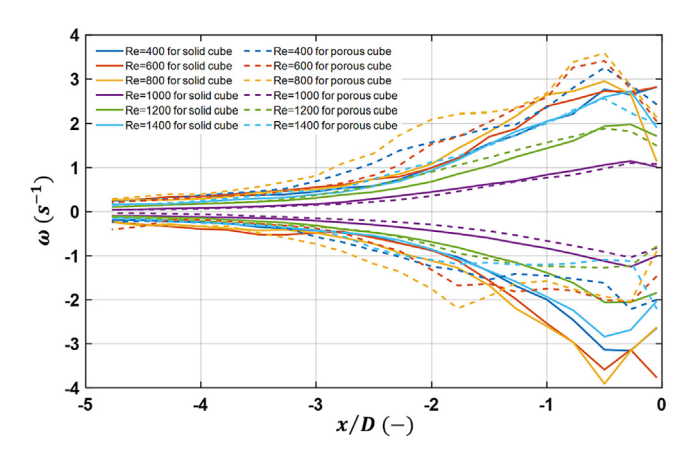


**Fig. 9.** Maximum and minimum vortices at various streamwise locations x/D for flow around the porous cube and solid cube at Re = 400,600,800,1000,1200,1400.

$$C_{D} = \frac{2}{Du_{\infty}^{2}} \int_{-H}^{+H} u_{avg} (u_{avg} - u_{\infty}) dy$$
 (1)

In this approach, contributions of the velocity fluctuation and pressure term are ignored. For a more complete calculation of the drag coefficient, the modified wake survey method (Bohl and Koochesfahani, 2009) is given as:

$$C_{D} = \frac{2}{D} \int_{-H}^{+H} \left[ \frac{u_{avg}}{u_{\infty}} \left( \frac{u_{avg}}{u_{\infty}} - 1 \right) + \varepsilon \left( \frac{u_{avg}}{u_{\infty}} - 1 \right) + \left( \frac{u_{r.m.s}}{u_{\infty}} \right)^{2} - \left( \frac{v_{r.m.s}}{u_{\infty}} \right)^{2} + \frac{1}{2} \left( 1 - \frac{u_{0}^{2}}{u_{\infty}^{2}} \right) \right] dy$$

$$(2)$$

In this equation, the first term is the momentum deficit due to the change of streamwise velocities, the second term is the correction for the slight variation of streamwise velocities along control surfaces when the integral distance H is not long enough, the third and fourth term is the velocity fluctuations accounting for instantaneous flow fields, and the last term is recovering  $u_0 \neq u_\infty$  effect when H is not far enough. Here, H is both long and far enough.

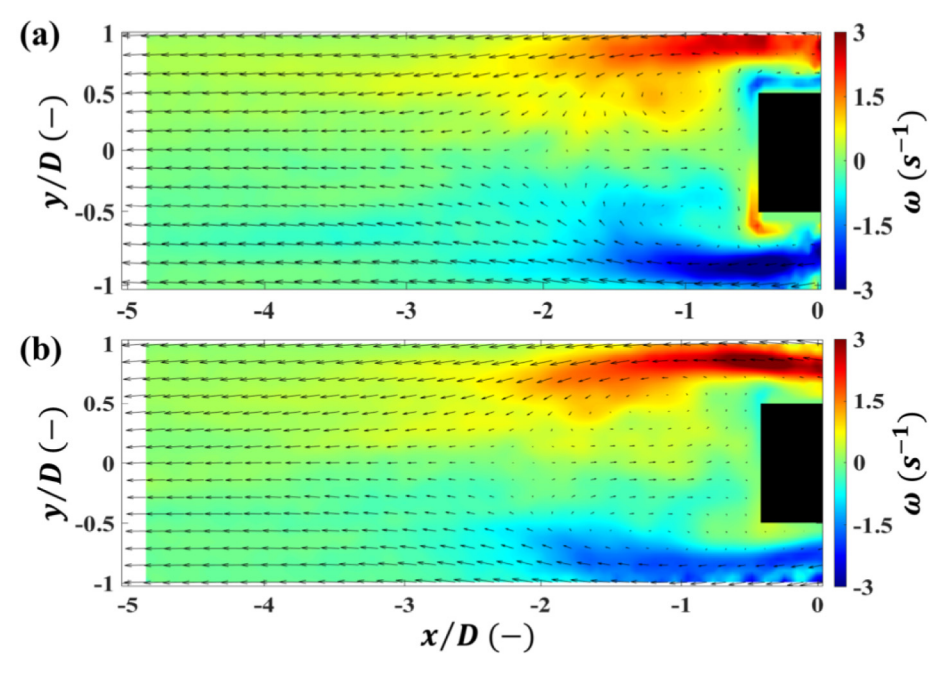


**Fig. 8.** Vorticity fields of (a) the solid cube and (b) the porous cube at Re = 1200.

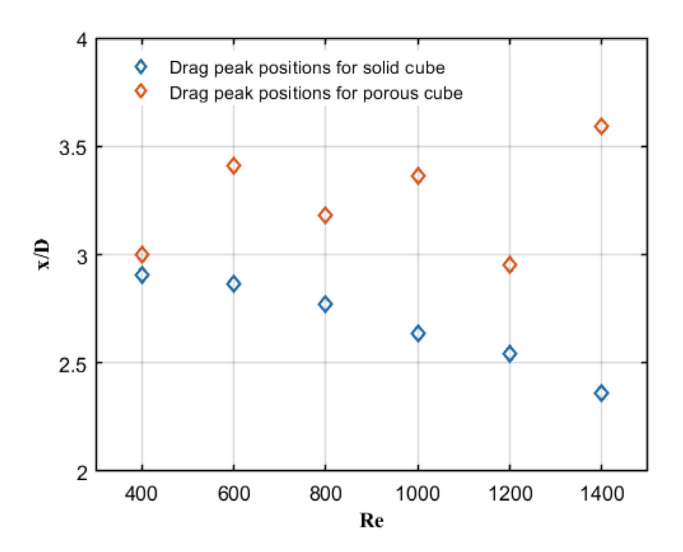


**Fig. 10.** Non-dimensional drag peak position x/D at various Reynolds numbers for the porous and solid cube.

It was found that there is a variation of calculated drag coefficients with the choice of integral positions x for H. In the present work, both for the solid cube case and the porous cube case, when the integral positions move from the near rear of the cube to the far downstream, the integral result always initially increases, then reaches a peak, and then decreases until it approaches zero for all experimental Reynolds numbers. The positions of the peak values for all cases are presented in Fig. 10. The peak phenomenon is chosen to be physically realistic and it can be explained that when integral positions x is within the recirculation wake for a near position from the cube, the two opposite vortices show an offset effect on the integration result. At a certain position near behind the stagnation point position, the integration result reaches the peak value. After that, the intensity of wake decreases and the flow gradually approaches the free stream at a far enough position.

As Fig. 10 shows, for the solid cube, non-dimensional drag peak positions x/D monotonously decrease with increasing Reynolds numbers, while there is a fluctuation without a clear trend for the porous cube. Drag peak positions x/D at all Reynolds numbers for the porous cube are larger than those of the solid cube, indicating a farther integral position for the porous cube due to its' larger recirculation region compared with the solid case at the same Re.

The positions of the peak values for each case were selected as the integral positions and comparisons of drag coefficients between the porous cube  $C_{D,p}$  and solid cube  $C_{D,s}$  at different Reobtained by Eq.(2) were provided in Fig. 11. Drag ratio is defined as  $C_{D,p}/C_{D,s}$ , and drag coefficients of porous and solid cube are same when drag ratio is equal to 1. As can be seen from Fig. 11, for lower Reynolds numbers (Re = 400.600.800), values of the drag ratios are less than 1 which means drag coefficients of the porous cube are slightly lower than those of the solid cube, whereas for higher Reynolds numbers (Re = 1000, 1200, 1400), drag ratios are larger than 1. This indicates that the drag coefficients of the porous cube are significantly higher than those of the solid cube. This result may have some similar inherent physics compared with the peak phenomenon found by Noymer et al. (1998). It was found by Noymer et al. (1998) that for intermediate values of Da around  $10^{-4} \sim 10^{-3},$  the drag ratio has a peak value which is more than 1 at higher Reynolds numbers, i.e. Re = 100 and 1000, for flow past a porous cylinder, representing an increase in drag compared with that of the solid case. However, for lower Reynolds numbers (i.e. Re = 10), there was no peak observed for all permeability values and the drag of the porous cylinder is lower than that of the solid

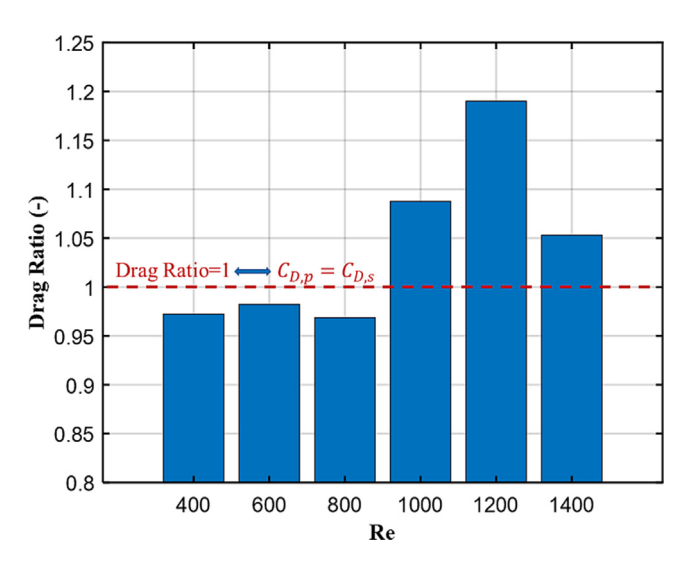


Fig. 11. Comparisons of drag coefficients between the porous and solid cube at different Re.

cylinder. Hence, as the finding in the previous work (Noymer et al., 1998), it was also observed that there was a similar trend in the range of  $400 \le Re \le 1400$  considered in the present work. The drag coefficients characterizing the drag force on the porous cube were decreased for a relative low Re flow and increased for a high Re flow. This may be due to the external flow around the cube is gradually transited to the internal flow through the porous cube with an increasing Re in presence of strong permeable effect.

Masliyah and Polikar (1980) also found that the increase of drag for the permeable body may be due to surface roughness. Nevertheless, it was also discussed by Noymer et al. (1998) that surface roughness might decrease the drag because roughness elements can promote the transition of flow to turbulent in the boundary layer and the turbulent boundary layer can postpone the occurrence of flow separation, which will reduce the drag coefficients as pressure drag is predominant at a higher Re. When the skinfriction drag is appreciable for a relatively low Re, the drag coefficients changed marginally. As discussed by Emadzadeh and Chiew (2020), flow permeation through porous particles can cause a smaller pressure drag corresponding to a lower  $C_D$ , while the roughness of porous particles can lead to a larger frictional drag corresponding to a higher  $C_D$ . It can be concluded that roughness effects on the increase of frictional drag may have nullified and exceeded permeability effects on the reduction of pressure drag at Re = 1000, 1200, 1400 in the present study. Thus, drag coefficients of the porous cube are significantly higher than those of solid cube for higher Reynolds (Re = 1000, 1200, 1400) in the present work. So, it can be argued the deviation of the drag coefficients of a porous cube from that of its solid counterpart might be due to these combining effects. That is, the transition of the external flow around solid cube to the internal flow through the porous cube in presence of permeability on the one hand, and the existence of the rough surface of a porous cube on the other hand.

#### 4. Conclusions

In this work, a PIV experimental investigation for wake characteristics and drag coefficients of flow around a high-permeability porous cube with  $Da=1.52\times10^{-3}$  was conducted. The model porous cubic particle used in the experiments is motivated by a newly developed fixed bed catalyst that is of a cubic and porous nature.

For comparison, parallel experiments with solid cube of similar size were also carried out.

The range of *Re* considered in the present work is from 400 to 1400. The measured area of the wake for the cube is nearly up to x/D = 5. The flow around the solid cube case was investigated by PIV to validate the experiment method. The effect of permeability on flow characteristics in the wake, including the instantaneous flow fields, time-averaged velocity field distributions, timeaveraged vorticity field distributions and drag coefficients, were presented to compare with the solid case. Recirculation region sizes in the wake were determined by the positions of stagnation points, which were identified by searching the local minimum value in the flow vector fields. For Re of 600  $\sim 1400$ , wake lengths of the porous cube are significantly increased compared with the solid cube, owing to the strong push effect of the penetration flow at a large permeability  $Da = 1.52 \times 10^{-3}$ . The variations of maximum and minimum vortices at various streamwise locations x/Dflow around the porous cube and solid cube at Re = 400,600,800,1000,1200,1400 are provided to show how the rotational effects evolve at the downstream of bluff bodies. A peak value of calculated drag coefficients was observed for all Re by varying integral positions based on the modified wake survey method (Bohl and Koochesfahani, 2009). At lower Reynolds numbers Re = 400,600,800, drag coefficients of the porous cube are slightly lower than those of the solid cube, whereas at higher Reynolds numbers Re = 1000, 1200, 1400, flow around and past the porous cube can arise an increase in drag compared with that of the solid case, and drag coefficients of the porous cube are significantly higher than those of the solid cube. This result indicates there may be some similar inherent physics underlying the flow past porous cube compared with the peak phenomenon for flow past the porous circular cylinder found by Noymer et al. (1998). This might be due to the transition of external flow around solid cube to the internal flow through the porous cube in the presence of permeability on the one hand, and the existence of rough surface of porous cube on the other hand. To our knowledge, this is the first full experimental work for flow around a porous cube. It is clearly shown that the effects of porous structure and shape of catalyst should be carefully considered in industrial reactors as it may alter the hydrodynamics.

#### CRediT authorship contribution statement

**Likun Ma:** Conceptualization, Methodology, Formal analysis, Investigation, Writing – original draft. **Sina Kashanj:** Validation, Formal analysis, Investigation. **Xue Li:** Formal analysis. **Shuliang Xu:** Resources. **David S. Nobes:** Resources, Writing – review & editing, Supervision. **Mao Ye:** Resources, Writing – review & editing, Supervision.

#### Data availability

Data will be made available on request.

#### **Declaration of Competing Interest**

The authors declare that they have no known competing financial interests or personal relationships that could have appeared to influence the work reported in this paper.

#### Acknowledgement

This work is part of a research program financially supported by the National Natural Science Foundation of China under Grant No. 21991093 and 22293021. We also thank the support of the scholarship from the University of Chinese Academy of Sciences (UCAS) for the Joint Training Program as a visiting scholar in University of Alberta in Canada.

#### References

- Atmakidis, T., Kenig, E.Y., 2009. CFD-based analysis of the wall effect on the pressure drop in packed beds with moderate tube/particle diameter ratios in the laminar flow regime. Chem. Eng. J. 155, 404–410.
- Augier, F., Idoux, F., Delenne, J.Y., 2010. Numerical simulations of transfer and transport properties inside packed beds of spherical particles. Chem. Eng. Sci. 65, 1055–1064.
- Bai, H., Theuerkauf, J., Gillis, P.A., Witt, P.M., 2009. A Coupled DEM and CFD Simulation of Flow Field and Pressure Drop in Fixed Bed Reactor with Randomly Packed Catalyst Particles. Ind. Eng. Chem. Res. 48, 4060–4074.
- Bhattacharyya, S., Dhinakaran, S., Khalili, A., 2006. Fluid motion around and through a porous cylinder. Chem. Eng. Sci. 61, 4451–4461. Bohl, D.G., Koochesfahani, M.M., 2009. MTV measurements of the vortical field in
- Bohl, D.G., Koochestahani, M.M., 2009. MTV measurements of the vortical field in the wake of an airfoil oscillating at high reduced frequency. J. Fluid Mech. 620, 63–88.
- Dixon, A.G., Walls, G., Stanness, H., Nijemeisland, M., Stitt, E.H., 2012. Experimental validation of high Reynolds number CFD simulations of heat transfer in a pilot-scale fixed bed tube. Chem. Eng. J. 200, 344–356.
- Emadzadeh, A., Chiew, Y.M., 2016. Settling velocity of a porous sphere. River Flow 2016, 555–562.
- Emadzadeh, A., Chiew, Y.M., 2020. Settling Velocity of Porous Spherical Particles. J. Hydraul. Eng. 146, 04019046.
- Guo, Q., Padash, A., Boyce, C.M., 2021. A two fluid modeling study of bubble collapse due to bubble interaction in a fluidized bed. Chem. Eng. Sci. 232, 116377.
- Hölzer, A., Sommerfeld, M., 2008. New simple correlation formula for the drag coefficient of non-spherical particles. Powder Technol. 184, 361–365.
- Jain, A.K., Basu, S., 2012. Flow Past a Porous Permeable Sphere: Hydrodynamics and Heat-Transfer Studies. Ind. Eng. Chem. Res. 51, 2170–2178.
- Joseph, D.D., Tao, L.N., 1964. The Effect of Permeability on the Slow Motion of a Porous Sphere in a Viscous Liquid. ZAMM Zeitschrift für Angewandte Mathematik und Mechanik 44, 361–364.
- Jurtz, N., Kraume, M., Wehinger, G.D., 2019. Advances in fixed-bed reactor modeling using particle-resolved computational fluid dynamics (CFD). Rev. Chem. Eng. 35, 139–190.
- Khan, M.H., Sooraj, P., Sharma, A., Agrawal, A., 2018. Flow around a cube for Reynolds numbers between 500 and 55,000. Exp. Therm Fluid Sci. 93, 257–
- Leal, L.G., 1989. Vorticity transport and wake structure for bluff bodies at finite Reynolds number. Phys. Fluids A 1, 124–131.
- Ma, L.K., Guo, Q., Li, X., Xu, S.L., Zhou, J.B., Ye, M., Liu, Z.M., 2022a. Drag correlations for flow past monodisperse arrays of spheres and porous spheres based on symbolic regression: Effects of permeability. Chem. Eng. J. 445, 136653.
- Ma, L.K., Kashanj, S., Xu, S.L., Zhou, J.B., Nobes, D.S., Ye, M., 2022b. Flow Reconstruction and Prediction Based on Small Particle Image Velocimetry Experimental Datasets with Convolutional Neural Networks. Ind. Eng. Chem. Res. 61, 8504–8519.
- Martin, S., 1981. Frazil ice in rivers and oceans. Annu. Rev. Fluid Mech. 13, 379–397. Masliyah, J.H., Polikar, M., 1980. Terminal velocity of porous spheres. Can. J. Chem. Eng. 58, 299–302.
- Matsumoto, K., Suganuma, A., 1977. Settling velocity of a permeable model floc. Chem. Eng. Sci. 32, 445–447.
- Mazaheri, K., Ebrahimi, A., Karimian, S., 2012. Performance Analysis of a Flapping-Wing Vehicle Based on Experimental Aerodynamic Data. J. Aerosp. Eng. 25, 45– 50
- Neale, G., Epstein, N., Nader, W., 1973. Creeping flow relative to permeable spheres. Chem. Eng. Sci. 28, 1865–1874.
- Noymer, P.D., Glicksman, L.R., Devendran, A., 1998. Drag on a permeable cylinder in steady flow at moderate Reynolds numbers. Chem. Eng. Sci. 53, 2859–2869.
- Reddy, R.K., Joshi, J.B., 2008. CFD modeling of pressure drop and drag coefficient in fixed and expanded beds. Chem. Eng. Res. Des. 86, 444–453.
- Saha, A.K., 2004. Three-dimensional numerical simulations of the transition of flow past a cube. Phys. Fluids 16, 1630–1646.
- Shahsavari, S., Wardle, B.L., McKinley, G.H., 2014. Interception efficiency in twodimensional flow past confined porous cylinders. Chem. Eng. Sci. 116, 752–
- Takeuchi, H., Tasaka, Y., Murai, Y., Takeda, Y., Tezuka, H., Mori, M., 2007. Particle Image Velocimetry for Air Flows Behind Permeable Cylinders. Fluids Eng. Divis. Summer Meeting 42886, 671–678.
- Topic, N., Agudo, J.R., Luzi, G., Czech, F., Wierschem, A., 2022. Shear-induced motion of a bead on regular substrates at small particle Reynolds numbers. J. Fluid Mech. 946, A45.
- Wang, J., 2020. Continuum theory for dense gas-solid flow: A state-of-the-art review. Chem. Eng. Sci. 215, 115428.
- Wei, X., Zhu, J., 2019. Capturing the instantaneous flow structure in gas-solid circulating fluidized bed using high-speed imaging and fiber optic sensing. Chem. Eng. Sci. 207, 713–724.
- Wittig, K., Nikrityuk, P., Richter, A., 2017. Drag coefficient and Nusselt number for porous particles under laminar flow conditions. Int. J. Heat Mass Transf. 112, 1005–1016.

- Wu, R.M., Lee, D.J., 1999. Highly porous sphere moving through centerline of circular tube filled with Newtonian fluid. Chem. Eng. Sci. 54, 5717–5722.
  Yu, P., Zeng, Y., Lee, T.S., Bai, H.X., Low, H.T., 2010. Wake structure for flow past and through a porous square cylinder. Int. J. Heat Fluid Flow 31, 141–153.
  Yu, P., Zeng, Y., Lee, T.S., Chen, X.B., Low, H.T., 2011. Steady flow around and through a permeable circular cylinder. Comput. Fluids 42, 1–12.
- Zhong, W., Yu, A., Liu, X., Tong, Z., Zhang, H., 2016. DEM/CFD-DEM Modelling of Non-spherical Particulate Systems: Theoretical Developments and Applications. Powder Technol. 302, 108-152.
- Zhu, L.T., Chen, X.Z., Luo, Z.H., 2021. Analysis and development of homogeneous drag closure for filtered mesoscale modeling of fluidized gas-particle flows. Chem. Eng. Sci. 229, 116147.